Nanoscale Advances

ROYAL SOCIETY OF CHEMISTRY

PAPER

View Article Online
View Journal | View Issue

Cite this: *Nanoscale Adv.*, 2025, **7**, 6066

Charge transport dynamics and energy storage implications of nickel cobalt carbonate hydroxide interaction with the *Aloe vera* leaf matrix

Kajal Gautam, *[a] Mohit Bhatt, [b] Archna Sagdeo,[cd] Hukum Singh[e] and Anil Kumar Sinha *[b]

Nanomaterial–plant interactions have recently emerged as a promising approach for modulating charge transport and energy storage behavior in living plant tissues. In this study, we report the first-time application of Nickel Cobalt Carbonate Hydroxide (NCCH) nanostructures to modulate the electrical properties of *Aloe vera* leaves. Uptake of transition metal oxides (TMOs) has enhanced or reduced seed germination, shoot/stem growth, and physiological and biochemical activities. However, NCCH nanoparticles (NPs) show improved redox behaviour compared to TMOs. The presence of CO_3^{2-} ions increases the wettability and ion transport. Well-characterized NCCH nanostructures were introduced at varying concentrations (1, 5, and 10 mg L^{-1}), and their influence on the impedance behavior of the plant was systematically examined. Electrochemical impedance spectroscopy data were modelled using an equivalent circuit comprising a parallel combination of resistance and capacitance for both intracellular (grain) and intercellular (grain boundary) regions of the leaves. The results showed a concentration-dependent increase in resistance and a decrease in capacitance across both domains, highlighting the significant modulation of charge mobility on uptake of NPs. The grain resistance increased from 2.83 Ω (control) to 8.1 Ω (10 mg L^{-1}) and the grain boundary resistance from 95.9 Ω to 299.74 Ω. Meanwhile, the capacitance decreased from 5.75 × 10^{-9} F to 2.15 × 10^{-9} F (grain) and from 1.38 × 10^{-10} F to 1.79 × 10^{-12} F (grain boundary), indicating a lower stored energy density but for a longer time in spiked plants. Jonscher's power law analysis revealed reduced hopping frequencies and altered carrier dynamics, especially in the grain boundary region, where the exponent dropped sharply at low concentrations. Modulus spectroscopy further confirmed the relaxation behavior influenced by NCCH uptake, with distinctive changes in M' and M'' profiles reflecting shifts in localized conduction and energy dissipation processes. These findings provide critical insights into the electrical modulation of plant tissues due to the uptake of transition metal nanostructures. This study not only expands the scope of plant nanobionics but also opens potential avenues for understanding the mechanism of plant defence against the toxicity of NPs and sustainable bioelectronics.

Received 2nd July 2025
Accepted 31st July 2025

DOI: 10.1039/d5na00651a

rsc.li/nanoscale-advances

1. Introduction

Nanomaterials have gained significant attention in recent years for their ability to interact with biological systems at the cellular and molecular levels.[1] When introduced into plants, these materials can enhance nutrient uptake,[2] improve water retention,[3] and influence various physiological processes.[4] Such enhancements are especially valuable for indoor plants, which often face limited access to natural sunlight and nutrients compared to outdoor counterparts.[5,6] Improving the functional properties of indoor plants can lead to better growth, increased stress tolerance,[7] and even potential applications in bioelectronics[8] and environmental monitoring.[9] Transition metal-based NPs, especially oxides, are found to enhance or reduce seed germination, shoot/stem growth, biomass production and physiological as well as biochemical activities.[10] NCCH nanoparticles (NPs) show improved redox behaviour compared to TMOs. The presence of CO_3^{2-} ions increases the wettability and ion transport.[11] Non-metallic nanomaterials, such as carbon-based nanoparticles, have been a major focus of research due to their biocompatibility,[12] chemical stability,[13] and ability to modulate plant physiological responses,[14] while metallic nanomaterials, particularly those based on transition metals,

[a]*Department of Chemistry, School of Advanced Engineering, UPES, Dehradun, India. E-mail: gautamkajal1210@gmail.com*

[b]*Department of Physics, School of Advanced Engineering, UPES, Dehradun, India. E-mail: anilksinha11@gmail.com*

[c]*Accelerator Physics & Synchrotron Utilisation Division, RRCAT, Indore, MP-452013, India*

[d]*HBNI, Training School Complex, Anushakti Nagar, Mumbai-248006, India*

[e]*ICFRE-Forest Research Institute, PO New Forest, Dehradun, 248006, India*

offer unique opportunities because of their rich electronic, catalytic, and redox properties.[15] Transition metals can actively participate in biological processes, potentially enhancing nutrient delivery, energy storage, and stress resistance in plants in ways that non-metallic nanomaterials cannot.[16] However, the mechanism underlying the plant defence against metal toxicity and other biological processes has not been well understood.

Transition metal-based nanomaterials offer a promising alternative, especially those involving nickel (Ni) and cobalt (Co), which exhibit variable oxidation states, rich redox chemistry, and strong catalytic properties.[17] Transition metal transporters are of central importance in the plant metal homeostasis network which maintains internal metal concentrations within physiological limits.[11] These features allow them to interact more dynamically with physiological processes in plants, potentially influencing electron transport, enzymatic functions, and intracellular charge mobility. Despite their established use in catalysis and energy storage,[18] such transition metal nanostructures remain underexplored in plant systems. In this context, *Aloe vera* was selected as the model plant due to its innate ability to thrive under arid conditions,[19,20] characterized by efficient water retention and energy storage in its thick, gel-like leaves.[21] These properties make it an ideal system for investigating how nanomaterials can influence internal charge transport and electrochemical behavior. Prior research has shown that carbon-based nanomaterials can affect such functions,[22] but the role of transition metal nanomaterials remains largely unknown.

This study introduces, for the first time, NCCH nanostructures as a functional material for modulating the electrochemical properties of *Aloe vera*. NCCH combines its high surface area and improved electrochemical activity with potential biocompatibility, presenting a unique candidate for enhancing plant performance.[18] We investigate the complex impedance response, charge transport characteristics, and energy storage behaviour of *Aloe vera* leaves treated with varying concentrations of NCCH. Our findings aim to expand the scope of plant nanobiotechnology by demonstrating the potential of transition metal nanomaterials to regulate physiological and electrical properties in living plants. To the best of our knowledge, this is the first report of NCCH NP interaction with plant systems, opening new directions for plant-based electronics, sustainable agriculture, and green energy storage.

2. Experimental

2.1 Synthesis of nickel cobalt carbonate hydroxide hydrate (NCCH)

NCCH was synthesized *via* a low-temperature hydrothermal method using aqueous precursors. The reagents used were nickel nitrate hexahydrate [$Ni(NO_3)_2 \cdot 6H_2O$] (8 mmol), cobalt nitrate hexahydrate [$Co(NO_3)_2 \cdot 6H_2O$] (4 mmol), urea [NH_2-$CONH_2$] (12 mmol), and ammonium hydroxide [NH_4OH] (2 mL), all of which were of analytical grade and used without further purification. Initially, nickel nitrate, cobalt nitrate, and urea were dissolved in 60 mL of deionized water under continuous stirring for 20 min to ensure a homogeneous solution. Following complete dissolution, 2 mL of ammonium hydroxide was added dropwise to the solution to maintain an alkaline pH, which is critical for controlled nucleation and growth of the desired hydroxide-carbonate phase and for tuning the morphology of the resulting nanomaterial. The solution was further stirred for 60 minutes to ensure uniform pH and reactant distribution. The resulting homogeneous solution was then transferred to a 100 mL stainless steel Teflon-lined autoclave and heated at 80 °C for 6 hours in a hot air oven to promote the hydrothermal reaction. Upon completion, the autoclave was allowed to cool to room temperature naturally.[18] The precipitate formed was collected by filtration using a Whatman filter paper (grade 42). The filtrate was carefully collected and stored separately for further use in plant treatment experiments, as presented in Fig. 1. The precipitate was first freeze-dried at −20 °C for 48 hours and subsequently placed in a lyophilizer to obtain a fine lyophilized powder.

The filtered solution obtained after the hydrothermal reaction was deliberately chosen for plant treatment experiments

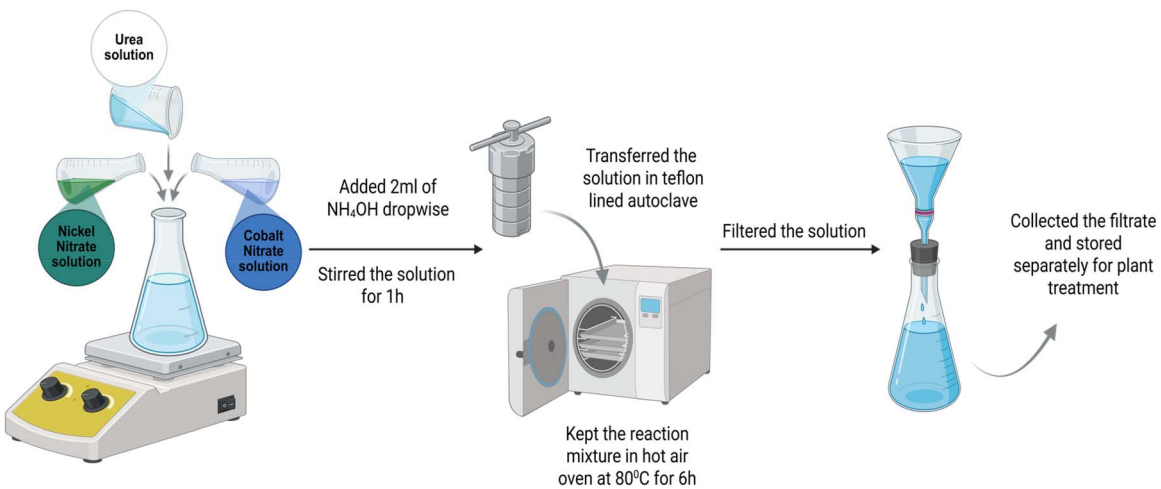

Fig. 1 Schematic diagram representing the synthesis procedure of NCCH nanomaterials.

due to its potential to contain ultrafine nanoparticles or ionic residues that were not captured by the Whatman filter paper during the separation process. The rationale behind this choice lies in the nano-biointeraction dynamics. Smaller-sized particles (often below 0.45 μm) or even metal ions are more likely to penetrate root tissues and translocate within plant systems due to their higher mobility and bioavailability. These nanofractions can pass through the root epidermis and reach the vascular tissues more efficiently compared to larger agglomerates or precipitated particles. Moreover, the filtrate may consist of colloidal nanoparticles, ionic species, or soluble complexes of nickel and cobalt, which mimic realistic environmental exposure conditions. By treating the plants with this filtered solution, the study aims to evaluate the potential uptake, transport, and biocompatibility of nanoscale components or ionic remnants in the plant system, offering insights into environmental nanotoxicology and potential nano-fertilizer applications.

2.2 Preparation of different concentration solutions

To study the dose-dependent response of *Aloe vera* to nanomaterial exposure, three different concentrations of the synthesized NCCH material were prepared. Accurately weighed amounts of lyophilized powder were dispersed in deionized water to form solutions of 1 mg L^{-1}, 5 mg L^{-1}, and 10 mg L^{-1} concentrations, respectively. Each solution was shaken well to ensure uniform dispersion of particles before use in the plant uptake experiment.

2.3 Treatment of *Aloe vera* with nanomaterial solutions

Aloe vera plants of similar age and size were selected for the study. The roots of each plant were gently washed with distilled water to remove any soil or debris. The plants were then individually placed in beakers containing the three prepared NCCH solutions (1 mg L^{-1}, 5 mg L^{-1}, and 10 mg L^{-1}). The treatment duration was maintained for 5 days, with the plant roots submerged directly in the nanomaterial solutions to allow uptake through the root system. The plants were kept under controlled room temperature and LED lighting conditions, ensuring a stable environment during the uptake process, as depicted in Fig. 2. 5 day exposure duration was selected based on previously reported studies,[23] where similar timeframes were sufficient to observe stable root uptake and physiological responses to ZnO nanoparticles. Additionally, uniform leaves were freshly harvested immediately after treatment to avoid post-harvest changes, and all measurements were conducted at room temperature (25 °C) to maintain consistency. After the 5 day treatment period, the plants were removed from the solutions, and the leaf sections were freshly cut for further experiments.

The concentrations 1, 5, and 10 mg L^{-1} for NCCH treatment were selected based on preliminary optimization as well as previously reported studies that highlighted potential phytotoxic effects of nanomaterials at higher concentrations. Multiple studies have shown that elevated concentrations of metal and metal oxide nanoparticles (beyond 10–20 mg L^{-1}) can induce oxidative stress, membrane disruption, and reduced growth in various plant systems. For instance, Chahardoli *et al.* demonstrated that engineered NiO nanoparticles at higher concentrations significantly inhibited root elongation and triggered antioxidant enzyme overexpression in *Nigella arvensis*.[24] A study by Nair *et al.*[25] concluded that increasing concentrations of transition metal nanoparticles, are associated with chlorosis, ROS accumulation, and biomass reduction in plants.[26] Similarly, in a reported study, *Aloe vera* was treated with carbon nanodots (CNDs), and even at a concentration of 10 mg L^{-1}, a significant increase in electrical resistance and reduced ionic mobility was observed, indicating stress-like responses within plant tissues.[22] These observations support our current approach of limiting the concentration range to 10 mg L^{-1} to avoid phytotoxic effects, maintain plant viability,

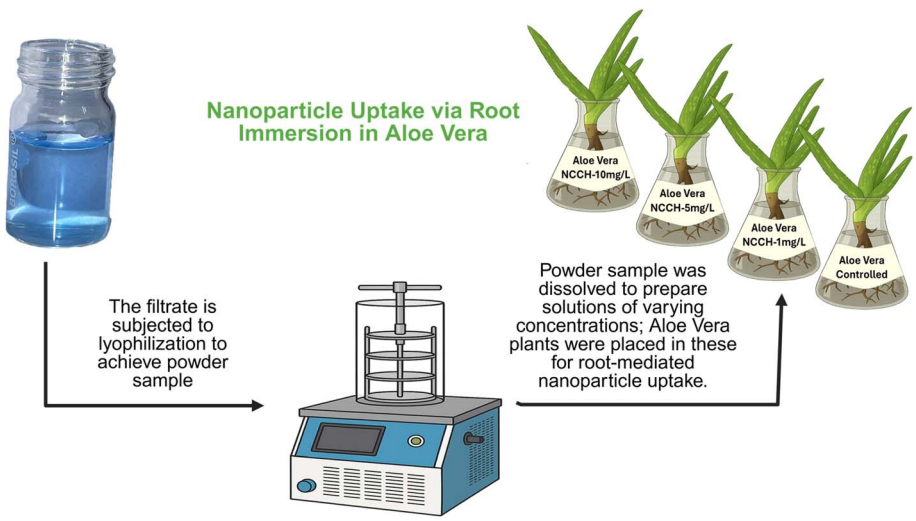

Fig. 2 *Aloe vera* plants after 5 day exposure to NCCH nanomaterial solutions at three concentrations: 1 mg L^{-1}, 5 mg L^{-1}, and 10 mg L^{-1}. Created with https://www.biorender.com/.

and ensure meaningful interpretation of electrochemical and bioelectronic interactions between the NCCH material and plant tissue.

2.4 Characterisation methods

2.4.1 Synchrotron X-ray diffraction (SXRD). Synchrotron X-ray diffraction (SXRD) analysis was carried out at the BL-12 beamline of the Indus-2 synchrotron facility in Indore, India. The measurements were performed in transmission mode using angle-dispersive XRD geometry. The samples were packed into rotating capillary tubes, and diffraction patterns were recorded using a MAR-345 dTB image plate area detector. A monochromatic X-ray beam with a wavelength of 0.8126 Å was obtained through a Si(111) double crystal monochromator. The sample-to-detector distance and wavelength calibration were done precisely using a LaB_6 NIST standard reference. The collected 2D diffraction images were processed and converted to $I(2\theta)$ plots using the Fit2D software.

2.4.2 Fourier transform infrared (FTIR) spectroscopy. FTIR spectroscopy (PerkinElmer Frontier, 500–4000 cm^{-1}) was performed to analyse the structural characteristics of the synthesized NCCH and treated plant samples. For the material, finely ground powder was mixed with spectroscopic-grade KBr and pressed into pellets. Plant samples, both control and treated, were dried at 50 °C until a constant weight and then pulverized. Baseline-corrected spectra confirmed the formation of the target material, identified residual functional groups, and evaluated molecular changes in the plant tissue post-treatment.

2.4.3 Electron microscopy. High-Resolution Transmission Electron Microscopy (HRTEM) was performed using a JEOL JEM 2100F (200 kV, LaB_6 filament) to examine the morphology and lattice structure of the NCCH materials. The images confirmed the nanoscale features and crystalline order.

2.4.4 AC impedance spectroscopy. AC impedance spectroscopy was carried out using a WAYNE KERR 6500B instrument at RRCAT, Indore, India, to evaluate the electrical properties of treated *Aloe vera* leaves. Leaves were rinsed with deionized water, sectioned into 1 × 1 cm pieces, and mounted in the sample holder for impedance analysis.

3. Results and discussion

3.1 X-ray diffraction (XRD) analysis

The crystalline structure of the as-synthesized NCCH was characterized using synchrotron-based X-ray diffraction (XRD) at BL-12, Angle Dispersive X-ray Diffraction (ADXRD) beamline, RRCAT, Indore, India, employing a high-resolution wavelength of 0.081262 nm. The diffraction pattern (Fig. 3) displays well-defined peaks indexed to the (100), (200), (310), (320), (501), and (511) planes, confirming the formation of a highly crystalline phase. These reflections are consistent with a hexagonal crystal structure belonging to the $P\bar{6}2m$ space group, as previously reported in crystallographic studies.[27]

The average crystallite size was estimated to be approximately 16 nm using the Scherrer formula (eqn (1)), indicating the nanocrystalline nature of the material.

$$D = \frac{k\lambda}{\beta \cos \theta} \quad (1)$$

where D is the average crystallite size, k is the shape factor (typically ~ 0.9, for spherical nanoparticles), λ is the X-ray wavelength (0.08126 nm), β is the full width at half-maximum (FWHM) of the diffraction peak (in radians), and θ is the Bragg angle (in radians).

3.2 Transmission electron microscopy (TEM) analysis

The morphology and particle size of the synthesized NCCH were analysed using transmission electron microscopy (TEM), as

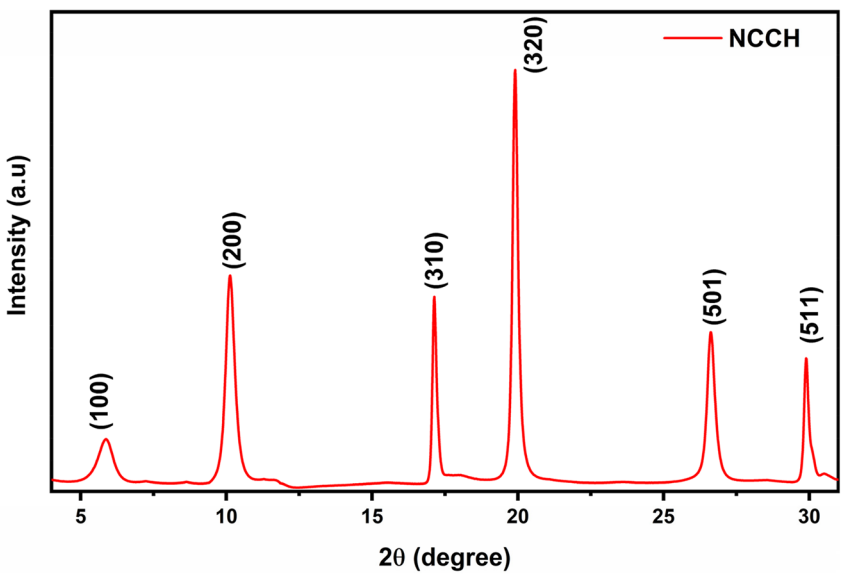

Fig. 3 Synchrotron XRD pattern of the NCCH sample (λ = 0.081262 nm). The diffraction peaks are indexed to the hexagonal phase with the space group $P\bar{6}2m$, confirming the high crystallinity and phase purity. The estimated crystallite size is ~16 nm based on the Scherrer formula.

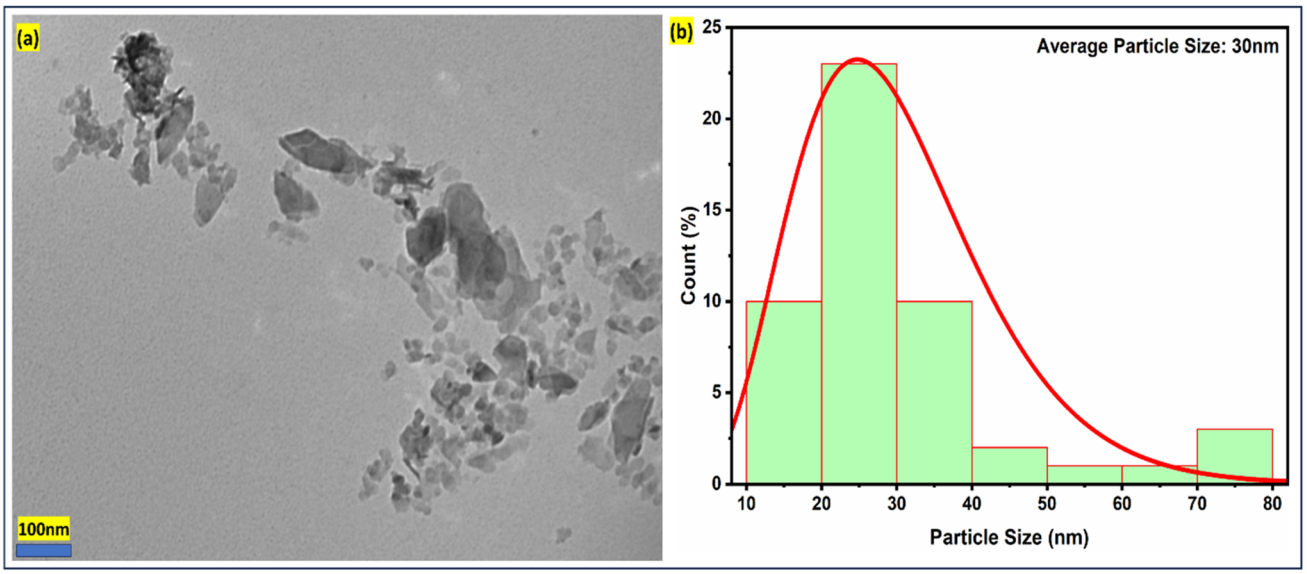

Fig. 4 (a) TEM micrograph and (b) particle size distribution histogram of NCCH nanoparticles in (DI) water. The particles exhibit a quasi-spherical morphology with moderate agglomeration. The average particle size is approximately 30 nm, making the material suitable for uptake through *Aloe vera* roots due to its favourable nanoscale dimensions.

shown in Fig. 4(a). The TEM image reveals that the particles possess a quasi-spherical to slightly elongated shape with a moderate degree of agglomeration. The nanostructures are relatively well-dispersed and fall within the expected nanoscale range. The particle size distribution histogram (Fig. 4(b)) shows that most of the particles range between 15 and 40 nm, with an average particle size of approximately 30 nm. This particle size range is particularly beneficial for plant-based applications. Nanomaterials with sizes below 50 nm are known to efficiently penetrate plant root systems through both apoplastic and symplastic pathways, facilitating internalization and transport.[28] Furthermore, previous studies have demonstrated the critical role of nanoparticle size in governing plant uptake and toxicity. For example, Lin and Xing (2008) reported that smaller ZnO nanoparticles (<50 nm) were more readily absorbed and translocated in ryegrass compared to larger counterparts, underscoring the importance of nanoscale dimensions for efficient uptake.[23] In this study, the synthesized NCCH nanostructures fall well within this favourable range, supporting their potential uptake through *Aloe vera* roots during root exposure treatments. The uniform nanoscale morphology not only enhances root permeability but also promotes better interaction with biological tissues, making NCCH a promising candidate for plant–nanomaterial interface studies.

3.3 Fourier transform infrared (FTIR) spectroscopy

3.3.1 Nickel cobalt carbonate hydroxide (NCCH). Fourier-transform infrared (FTIR) spectroscopy was performed to investigate the chemical functionalities present in the synthesized NCCH, as depicted in Fig. 5(a). The spectrum reveals several well-defined absorption bands, which provide insights into the molecular structure and bonding within the material. Notably, the overall pattern closely resembles that of zaratite, indicating structural similarities.[29] A broad absorption band centred around 3400 cm^{-1}, with peaks at 3524, 3410, 3289, and 3082 cm^{-1}, is characteristic of O–H stretching vibrations. The peaks at 3524 and 3410 cm^{-1} can be attributed to water molecules associated with carbonate species ($CO_3^{-}\cdot H_2O$), while those at 3289 and 3082 cm^{-1} are linked to the presence of $(CO_3)^{2-}\cdot H_2O$ complexes.[30] These features confirm the involvement of hydrated carbonate groups in the NCCH matrix. Similar O–H stretching bands are commonly observed in nickel hydroxide, suggesting the coexistence of hydroxyl groups in the structure.[31] The region near 1400 cm^{-1} displays strong absorption at 1472 and 1378 cm^{-1}, which is attributed to the asymmetric stretching vibrations of carbonate ions (CO_3^{2-}), further supporting their incorporation into the compound.[32] In the lower wavenumber region, distinct peaks are observed at 697, 606, 528, and 440 cm^{-1}. These are assigned to stretching vibrations of transition metal–oxygen (TM–O) bonds, which are indicative of metal–ligand coordination within the layered framework.[33] Additional bands appearing below 1000 cm^{-1} are associated with both TM–O stretching and TM–O–H bending modes, suggesting the presence of both metal–oxygen and metal–hydroxyl interactions.[34] Overall, the FTIR spectrum confirms the presence of key structural components in NCCH, including hydroxyl groups, carbonate anions, coordinated water, and metal–oxygen bonds.

3.3.2 *Aloe vera*. FTIR spectroscopy was employed to examine the changes in functional group vibrations in *Aloe vera* leaves following treatment with NCCH nanoparticles at concentrations of 1 mg L^{-1}, 5 mg L^{-1}, and 10 mg L^{-1}. As shown in Fig. 5(b), the spectra reveal characteristic absorption bands corresponding to native biomolecules, with notable changes observed across treated and untreated samples, indicating interactions between the plant matrix and the nanoparticles.

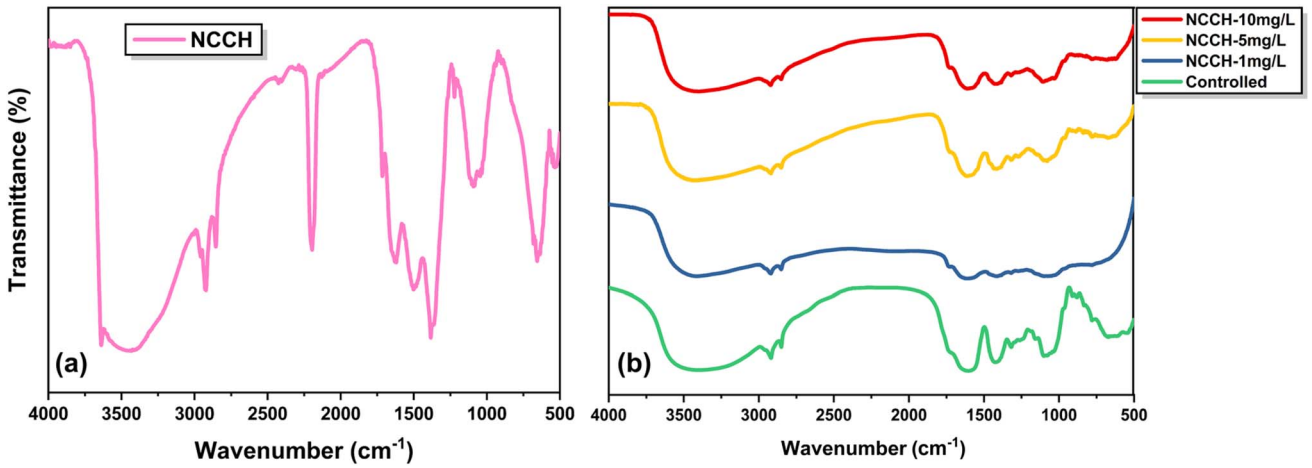

Fig. 5 FTIR spectra of (a) synthesized NCCH nanostructures, confirming the presence of characteristic functional groups and (b) *Aloe vera* leaves treated with different concentrations of NCCH (1 mg L^{-1}, 5 mg L^{-1}, and 10 mg L^{-1}) compared to the untreated control, showing changes in transmittance patterns indicative of nanoparticle-induced biochemical interactions.

FTIR spectra of all the samples, including the control sample, exhibit a broad band in the region of 3560–3200 cm^{-1}, centred around 3366 cm^{-1}, attributed to O–H stretching vibrations. This region is typically associated with hydroxyl groups in phenolic compounds and carboxylic acids.[35,36] In the nanoparticle-treated samples, especially at 10 mg L^{-1}, this band shows noticeable broadening and decreased transmittance. Such spectral changes suggest enhanced hydrogen bonding interactions and increased water retention in the plant tissue,[37] possibly due to the hydrophilic nature of NCCH nanoparticles, which contain –OH and carbonate functionalities capable of interacting with water and native plant biomolecules.[38] The C–H stretching region around 2919 cm^{-1}, along with a shoulder near 2853 cm^{-1}, remains visible across all spectra. These bands are linked to symmetric and asymmetric stretching of methylene groups.[35,39] While present in both control and treated samples, slight shifts and intensity variations in treated samples may indicate mild structural modifications in aliphatic chains due to nanoparticle exposure. A peak at approximately 1586 cm^{-1}, attributed to C=C aromatic ring stretching and possibly asymmetric stretching of carboxylate groups,[36] is observed in all samples. However, this band is more defined in the control, while its intensity appears slightly reduced in NCCH-treated leaves, possibly due to complexation or partial masking of these groups by metal ions or changes in local pH near the tissue surface. Similarly, the band near 1415 cm^{-1}, characteristic of symmetric carboxylate stretching,[40] is retained in all samples but shows a downward shift and broadening with increased NCCH concentration, implying potential coordination of carboxylate groups with Ni^{2+} or Co^{2+} ions from the nanoparticles. In the fingerprint region, an intense band near 1099 cm^{-1}, representing C–O and C–OH stretching in glucans and other polysaccharides, is clearly visible in all samples.[41] A shoulder at ~1161 cm^{-1} suggests the presence of pectic side chains.[42] These peaks become broader and less intense in the treated samples, particularly at 10 mg L^{-1}, which may indicate disruption or crosslinking in the polysaccharide matrix, possibly affecting the hydration and structural conformation of the cell wall. Lower wavenumber bands below 1000 cm^{-1}, especially around 800–600 cm^{-1}, show increasing intensity with NCCH concentration, which could be attributed to the presence of metal–oxygen (TM–O) stretching vibrations from the nanoparticle residues adhering to or interacting with plant tissues. Overall, the FTIR analysis confirms that while the primary biomolecular features of *Aloe vera* are preserved, treatment with NCCH nanoparticles leads to subtle but consistent modifications in hydroxyl-, carboxyl-, and polysaccharide-associated regions. These changes suggest physical and chemical interactions at the plant–nanoparticle interface, which could influence water retention, structural integrity, and possibly metabolic activity in the leaves.

3.4 AC impedance spectroscopy and equivalent circuit modelling

Complex impedance $Z = R + jX$, where R represents the resistance and X denotes the reactance, serves as a valuable parameter for probing the electrical characteristics of plant tissues.[43] In *Aloe vera*, the mid to high-frequency electrical response is governed primarily by intracellular (mid-frequency) and extracellular (high frequency) conduction pathways, referred to as symplastic and apoplastic conduction, respectively.[44,45] These mechanisms are analogous to grain and grain boundary conduction observed in ceramic materials. Low frequency conduction represents the conduction pathways of the surface and the contact.

AC impedance spectroscopy of *Aloe vera* treated with varying concentrations of NCCH nanoparticles reveals a non-monotonic response in both impedance magnitude and phase behavior, highlighting a complex interplay between nanoparticle concentration and charge transport dynamics within plant tissues.[46] In Fig. 6(a), the 5 mg L^{-1}-treated sample exhibits the highest impedance in the low-frequency regime, suggesting substantial suppression of ionic or electronic conductivity. This

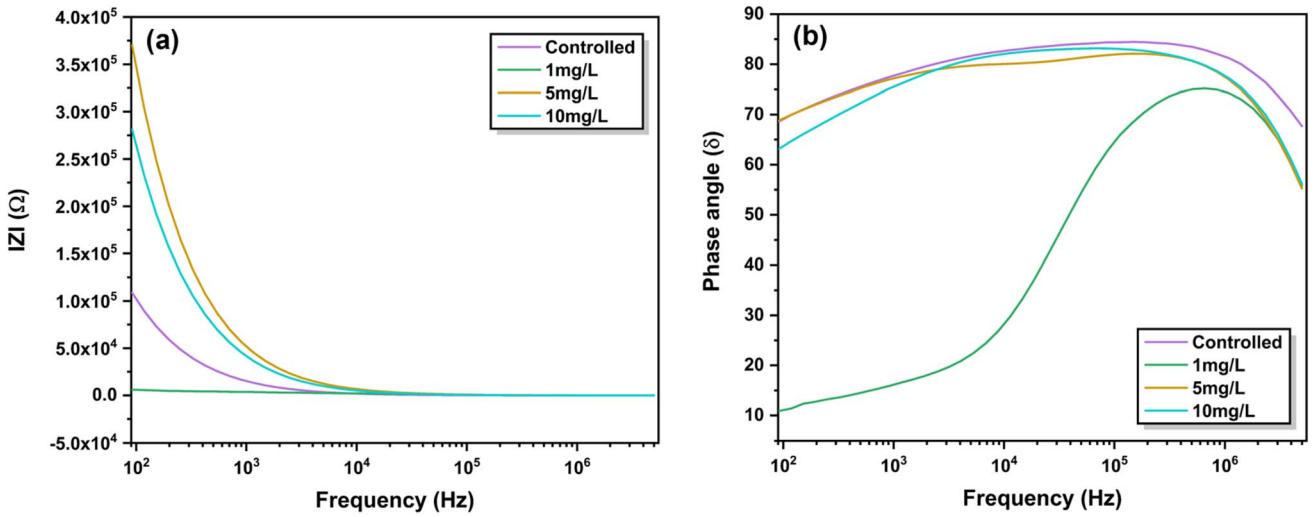

Fig. 6 Frequency-dependent behavior of the impedance modulus $|Z|$ (a) and phase angle δ (b) for untreated (control) *Aloe vera* leaves and those treated with various concentrations (1 mg L^{-1}, 5 mg L^{-1}, and 10 mg L^{-1}) of NCCH *via* root uptake.

anomalous increase in impedance may result from nanoparticle agglomeration or partial blockage of intrinsic conduction pathways, introducing interfacial barriers or disrupting native tissue conductivity. The 10 mg L^{-1}-treated sample shows moderately reduced impedance relative to the 5 mg L^{-1}-treated sample but still exceeds that of the control, indicating that although the nanoparticle integration may be more uniform at this concentration, it has not yet achieved optimal conductive enhancement. Notably, the 1 mg L^{-1}-treated sample exhibits the lowest impedance across the frequency spectrum, outperforming both the control and higher-concentration treatments. In the high-frequency region, $|Z|$ becomes frequency-independent, with the control, 1 mg L^{-1}-treated, and 10 mg L^{-1}-treated samples showing comparable values. A slightly elevated $|Z|$ is observed for the 5 mg L^{-1}-treated sample in this region. At lower frequencies, the impedance modulus $|Z|$ increases progressively, indicating enhanced resistance to charge transport due to nanoparticle accumulation within the plant matrix. The profile resembles the impedance response of ionically conductive systems or hydrated biological matrices. The phase angle plots show a gradual rise to a peak, followed by a decline with further frequency increase (Fig. 6(b)). This behavior is indicative of interfacial polarization and ionic motion within the plant tissues. The data suggest that the internal structure of the *Aloe vera* leaf, influenced by NCCH treatment, supports a combination of bulk ionic conduction and interfacial effects that dominate at lower frequencies.

The Nyquist plot is the plot between reactance ($-X$) and resistance (R), which shows semi-circular arcs in high- and mid-frequency regions, corresponding to grain and grain boundary conductions, respectively. The Nyquist plots for the controlled and the 10 mL samples are shown in Fig. 7(a) and (b), respectively. The sample reveals a well-resolved semicircular arc, characteristic of a dominant bulk relaxation process, followed by a low-frequency tail indicative of interfacial polarization

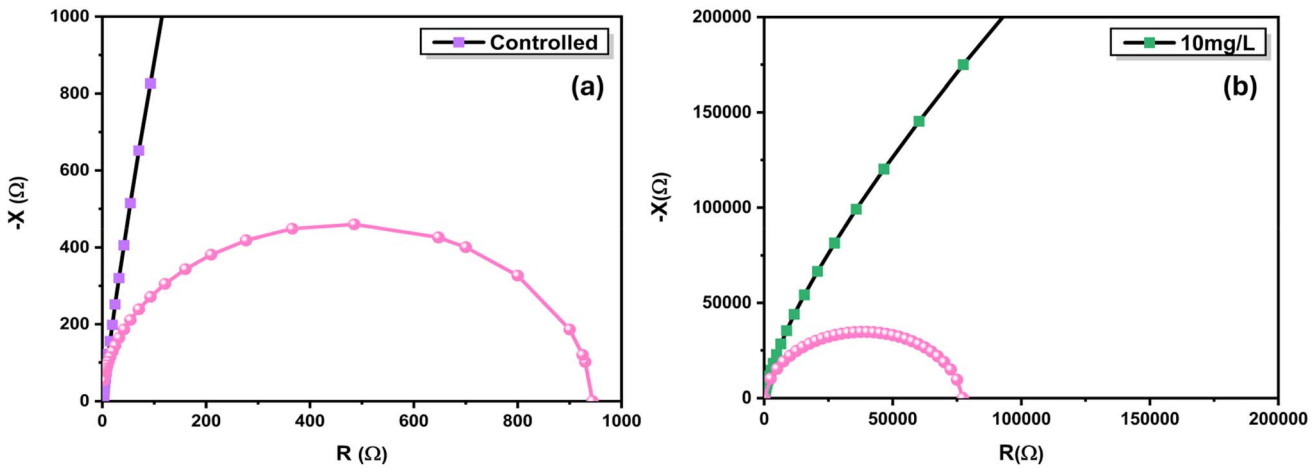

Fig. 7 Nyquist plot (Z' *vs.* $-Z''$) of the (a) controlled sample and (b) 10 mg L^{-1}-treated sample recorded at room temperature.

phenomena.[47] The figures also show the semicircular arcs corresponding to grain conduction, in each case.

The extracted centre coordinates of the arc are (470.9, −13.5) and (38 634, −4119), respectively, for the control and 10 mL samples. The canters of the semicircles in the fourth quadrant suggest deviation from ideal capacitive behavior, typically attributed to surface roughness, inhomogeneity, or a distribution of relaxation times.[48] Thus, the resistance and capacitance of the AC electric circuit are replaced by constant phase elements for further analysis. The resistances of the grain of the control and 10 mL samples are found to be 942 Ω and 77 kΩ, respectively. The semicircle arcs in the mid-frequency range data were also fitted (not shown in the figure) to estimate the resistances of the grain boundary. The grain boundary resistances of the control and 10 mL samples were found to be 115.6 kΩ and 171.9 kΩ, respectively. We find a very large increase in the resistance of the grain region (intercellular), whereas the resistance of the intracellular conduction remains unchanged. So, the effect of NCCH uptake is more pronounced in intercellular conduction. These impedance characteristics collectively underscore the influence of microstructural and interfacial features on charge transport in the controlled system. However, a CPE-based circuit model for quantitative analysis is required to fully understand the change in energy storage as well as transport on NP uptake. To interpret the impedance behavior of the plant-based system, a simplified equivalent circuit comprising two $R\|C$ units connected in series was employed, as shown in Fig. 8. This minimal configuration effectively captures the dominant charge transport processes occurring within the biological tissue. The first $R_1\|C_1$ unit is attributed to the intracellular/grain resistance (R_1) and associated pseudo-capacitive behavior, modeling ion migration and polarization within individual cells primarily across the cytoplasm and vacuole compartments. The second $R_2\|C_2$ branch represents the intercellular/grain boundary resistance (R_2) and capacitive effects associated with the cell-to-cell junctions, including contributions from the plasmodesmata, apoplastic spaces, and the cell wall matrix.

When the centre of the Nyquist semicircle lies below the x-axis, the system shows non-ideal Debye-type behavior, which indicates a deviation from ideal capacitive or resistive responses.[49] In such cases, conventional circuit elements such as resistance and capacitance are replaced with a Constant Phase Element (CPE) to better represent the charge transport behavior.[50] The impedance is then expressed using the CPE-based impedance function (eqn (2)):[45]

$$Z_{\mathrm{CPE}} = {A_{\mathrm{CPE}}}^{-1}(j\omega)^{-n}. \tag{2}$$

In the equivalent circuit, the constant phase element (CPE) is characterized by two parameters: the frequency-independent pre-exponential factor A_{CPE} and the empirical exponent n, which govern the degree of deviation from ideal capacitive behavior. The value of n typically ranges between 0 and 1, where $n = 0$ corresponds to a purely resistive response with an impedance $Z_\theta = \dfrac{1}{A_{\mathrm{CPE}}}$, while $n = 1$ reflects ideal capacitive behavior, yielding $Z_\theta = \dfrac{-1}{A_{\mathrm{CPE}}\omega}$.[51,52]

For grain,

$$Z_{\mathrm{CPE}} = Z^{(\mathrm{g})}_{\mathrm{CPE}} + Z^{(\mathrm{gB})}_{\mathrm{CPE}}. \tag{3}$$

$$Z^{\mathrm{g}}_{\mathrm{CPE}} = (A^{\mathrm{g}}_{\mathrm{CPE}})^{-1}\omega^{-n_1}\mathrm{j}^{-n_1}. \tag{4}$$

$$|Z|^{\mathrm{g}}_{\mathrm{CPE}} = (A^{\mathrm{g}}_{\mathrm{CPE}})^{-1}\omega^{-n_1}. \tag{4a}$$

Similarly, for the grain boundary,

$$Z^{\mathrm{gB}}_{\mathrm{CPE}} = (A^{\mathrm{gB}}_{\mathrm{CPE}})^{-1}\omega^{-n_1}\mathrm{j}^{-n_1}$$

$$|Z|^{\mathrm{gB}}_{\mathrm{CPE}} = (A^{\mathrm{gB}}_{\mathrm{CPE}})^{-1}\omega^{-n_1}. \tag{4b}$$

To further elucidate the frequency-dependent electrical response of the *Aloe vera* system under varying concentrations of NCCH nanoparticles, Bode plots of absolute impedance ($|Z|$) were analysed across a broad frequency spectrum (10^2 to 10^6 Hz). The $|Z|$ *vs.* frequency profiles, as depicted in Fig. 9, reveal three distinct regions: Region-I (10^2 to 10^4 Hz), Region-II (10^4 to 10^6 Hz), and Region-III (above 10^6 Hz), each corresponding to different structural components of the biological matrix. Region-I reflects the impedance arising from the electrode–sample interface and contact resistances, dominated by polarization and ion accumulation at the interface. Region-II is attributed to grain boundary effects, capturing the resistive and capacitive interplay at intercellular junctions such as plasmodesmata and apoplastic pathways. Region-III corresponds to the intrinsic grain or intracellular response, where the impedance is primarily governed by ionic motion within the cytoplasm and vacuole compartments.

In Region-I, a pronounced elevation in $|Z|$ is observed with increasing nanoparticle concentration, indicating enhanced polarization effects and restricted ionic mobility. Region-II corresponds to the transition zone where capacitive and resistive effects co-exist, reflecting contributions from both intercellular junctions and the cytoplasmic matrix. Notably, samples

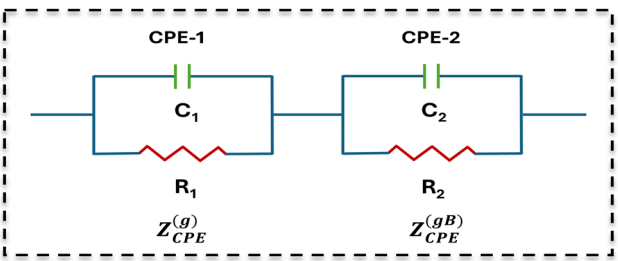

Fig. 8 Equivalent circuit model used to fit the impedance spectra of the plant-based system. The model comprises two $R\|C$ elements in series: the first $R_1\|C_1$ corresponds to intracellular resistance and capacitive dispersion within the cellular compartments (grain), while the second $R_2\|C_2$ represents the intercellular resistance and charge storage across cell junctions, including plasmodesmata and apoplastic pathways (grain boundary).

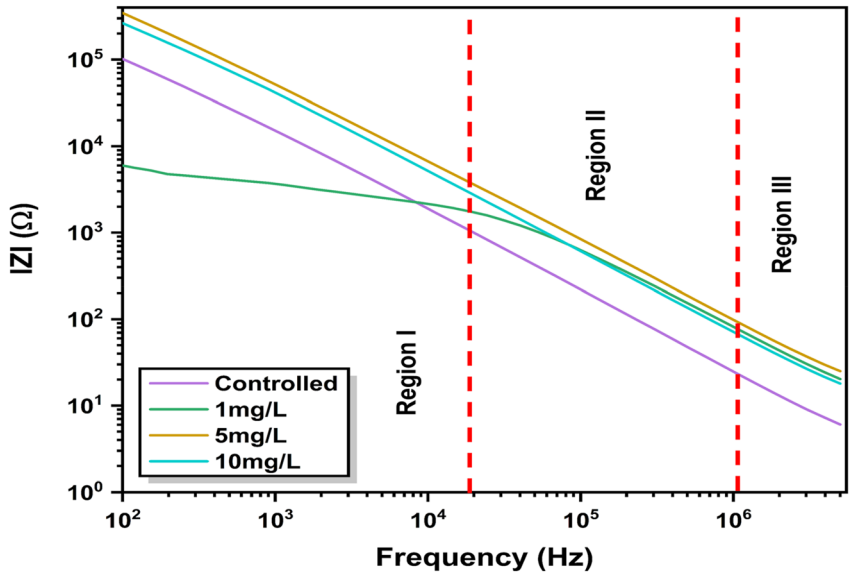

Fig. 9 Frequency-dependent Bode plot (|*Z*| *vs.* frequency) for *Aloe vera* tissues treated with varying concentrations of NCCH nanoparticles (1 mg L^{-1}, 5 mg L^{-1}, and 10 mg L^{-1}) compared to the untreated control.

treated with 5 mg L^{-1} and 10 mg L^{-1} NCCH exhibit similar impedance trends in this region, suggesting a saturation threshold in their influence on tissue conductivity. In Region-III, the impedance magnitude decreases sharply and converges across all concentrations, indicative of minimal capacitive resistance at high frequencies where dielectric relaxation dominates. Anomalous behavior is notably observed in the 1 mg L^{-1}-treated sample, which exhibits a sharp deviation from the monotonic trend seen in higher concentrations. In Region-I, this sample displays significantly lower impedance, suggesting facilitated charge transfer or enhanced electrolyte penetration at the interface. Such non-linear behavior may be indicative of sub-lethal ionic stress or transient membrane permeability changes triggered by low-dose nanoparticle interaction, effects that are absent or suppressed at higher dosages, possibly due to compensatory physiological adaptations.

The complex impedance measurements were interpreted through a modified brick-layer model. This model accounts for the heterogeneous structure of plant tissues by representing the system as a series of intercellular (grain boundary) and intracellular (grain) domains.[53] The impedance spectra were fitted using constant phase elements (CPEs) to accurately capture the non-ideal capacitive characteristics intrinsic to biological matrices. From the extracted CPE parameters, namely the pre-exponential factor (A) and the dispersion exponent (n), the corresponding resistance (R_{CPE}) and pseudo-capacitance (C_{CPE}) values were derived in Table 1 using the following established analytical expressions:

$$Z_{CPE} = \frac{1}{A_{CPE}} \frac{1}{(j\omega)^n}$$

$$Z_{CPE} = \frac{1}{A_{CPE}\omega^n}(-j)^n = \frac{1}{A_{CPE}\omega^n}\left(\cos\frac{\pi n}{2} - j\sin\frac{\pi n}{2}\right)$$

Or

$$Z_{CPE} = R_{CPE} + jX_{CPE} = \frac{1}{A_{CPE}\omega^n}\left(\cos\frac{\pi n}{2} - j\sin\frac{\pi n}{2}\right) \quad (5)$$

$$R_{CPE} = \frac{1}{A_{CPE}\omega^n}\cos\frac{\pi n}{2}. \quad (5a)$$

$$X_{CPE} = \frac{-j}{\omega_{CPE}} = \frac{-j}{A_{CPE}\omega^n}\left(\sin\frac{\pi n}{2}\right)$$

Therefore,[54,55]

Table 1 Grain and grain boundary CPE equivalent circuit parameters

	(g)		(gB)		(g)	(gB)	(g)	(gB)
Sample	A_{CPE}	n_1	A_{CPE}	n_2	C_{CPE} (farad)	C_{CPE} (farad)	R_{CPE} (Ω)	R_{CPE} (Ω)
Control	7.90×10^{-8}	0.84 ± 0.01	1.58×10^{-8}	$0.94 \pm 7 \times 10^{-4}$	5.75×10^{-9}	1.38×10^{-10}	2.83	95.90
1 mg L^{-1}	1.99×10^{-8}	0.85 ± 0.01	1.25×10^{-8}	0.87 ± 0.006	1.70×10^{-9}	2.77×10^{-9}	8.97	594.80
5 mg L^{-1}	3.14×10^{-8}	0.81 ± 0.01	5.48×10^{-9}	0.92 ± 0.0016	1.41×10^{-9}	4.81×10^{-12}	13.89	46.60
10 mg L^{-1}	3.47×10^{-8}	0.83 ± 0.01	6.63×10^{-9}	$0.93 \pm 8.6 \times 10^{-4}$	2.15×10^{-9}	1.79×10^{-12}	8.10	299.74

$$C_{CPE} = \frac{A_{CPE}\omega^{n-1}}{\sin\frac{\pi n}{2}}. \quad (5b)$$

The CPE exponent n, indicative of the deviation from ideal capacitive behavior, remained relatively stable in the grain region, ranging narrowly from 0.84 (control) to 0.81 (5 mg L^{-1}) and reverting to 0.83 at the highest concentration. This consistency reinforces the notion that intracellular charge storage mechanisms are resilient to moderate external perturbations. In contrast, the grain boundary n values exhibited greater sensitivity to treatment. A substantial reduction from 0.94 (control) to 0.87 was observed at 1 mg L^{-1}, followed by a progressive increase at 5 mg L^{-1} (0.92) and 10 mg L^{-1} (0.93). This trend highlights a concentration-dependent restructuring of intercellular ionic channels, possibly driven by the dynamic interaction of nanoparticles with cell wall polysaccharides and mucilaginous layers. Pseudo-capacitance (C_{CPE}) values further revealed the influence of NCCH exposure on the dielectric nature of the tissues. Within the grain region, C_{CPE} showed a clear decreasing trend from 5.75×10^{-9} F in the control to 2.15×10^{-9} F at 10 mg L^{-1}, suggesting reduced intracellular polarizability and potential alterations in cytoplasmic composition or ion mobility. Notably, the grain boundary C_{CPE} displayed a dramatic decline, dropping from 1.38×10^{-10} F to 1.79×10^{-12} F, reinforcing the hypothesis of impaired water content or hindered ionic diffusion within the extracellular matrix. These changes in capacitance point to a nanoparticle-induced modulation of the tissue's dielectric landscape, particularly within the intercellular continuum.

The resistance component (R_{CPE}) mirrored these dielectric modifications. Intracellular resistance escalated significantly from 2.83 Ω (control) to a peak of 13.89 Ω at 5 mg L^{-1} before subsiding to 8.1 Ω at 10 mg L^{-1}. This suggests initial obstruction in electron or ion migration pathways due to particle-induced reorganization, with partial conductivity restoration at higher concentrations. Meanwhile, the grain boundary resistance fluctuated more intensely. A sharp rise to 594.8 Ω at 1 mg L^{-1} was followed by a substantial drop to 46.6 Ω at 5 mg L^{-1} and a resurgence to 299.74 Ω at 10 mg L^{-1}, pointing to complex interactions governing extracellular ionic permeability. The amplitude factor A_{CPE} for both regions further supports this interpretation. In the grain domain, A decreased by approximately 56% (from 7.9×10^{-8} to 3.47×10^{-8} F s^{n-1}), while the grain boundary domain experienced a comparable decline of about 58% (from 1.58×10^{-8} to 6.63×10^{-9} F s^{n-1}). These reductions reflect a marked decline in electrochemical activity and increased structural heterogeneity, likely associated with nanoparticle accumulation and its influence on the conduction framework of *Aloe vera* tissues. These findings provide strong evidence that NCCH nanoparticles might modulate both capacitive and resistive elements of biological impedance in a concentration-specific manner.

3.5 Dielectric response

The dielectric response and AC conductivity analyses offer critical insights into the intrinsic electrical behavior of *Aloe vera* tissues independent of their macroscopic geometry.[56] Unlike the resistance (R) and reactance (X), which can be influenced by sample dimensions, dielectric parameters are material-specific and governed by the polarization and charge transport

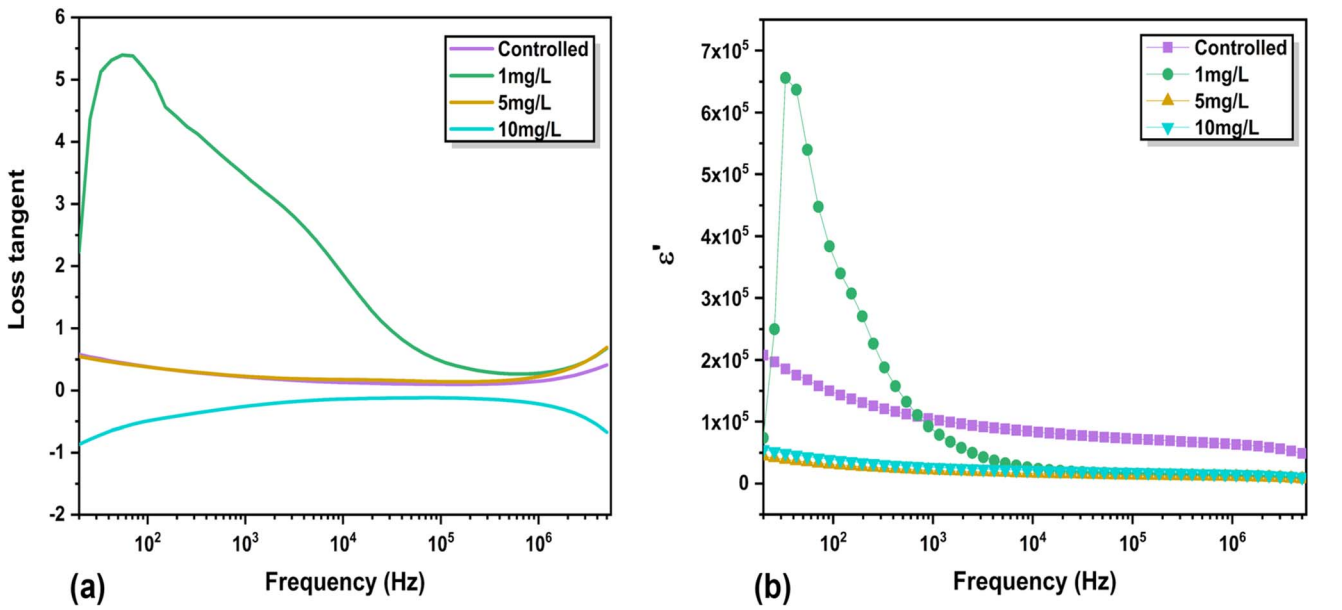

Fig. 10 Frequency-dependent (a) loss tangent and (b) real part of dielectric constant (ε') for *Aloe vera* leaves treated with varying concentrations of NCCH (1 mg L^{-1}, 5 mg L^{-1}, and 10 mg L^{-1}) compared to the untreated control. The data reveal significant modification in dielectric response and energy dissipation behavior, particularly at lower frequencies, indicating altered charge storage and transport mechanisms upon nanoparticle treatment.

mechanisms within the tissue microstructure. The frequency-dependent complex permittivity, expressed as $\varepsilon = \varepsilon' + i\varepsilon''$, captures both energy storage (ε') and dissipation (ε'') characteristics under an alternating electric field.[57] These components are derived from impedance spectra using the relation:[58]

$$\varepsilon' = \frac{X}{|Z|^2 \omega C_0} \text{ and } \varepsilon'' = \frac{R}{|Z|^2 \omega C_0}$$

where ω is the angular frequency, $|Z|$ is the magnitude of complex impedance, and C_0 denotes the vacuum capacitance of an equivalent parallel-plate capacitor, defined as:

$$C_0 = \frac{\varepsilon_0 a}{d}$$

where ε_0 is the permittivity of free space, a represents the effective electrode area in contact with the sample, and d is the sample thickness.

The dielectric constant (ε') of *Aloe vera* plants treated with different NCCH nanoparticle concentrations plotted as a function of frequency is shown in Fig. 10(b). In the control sample, ε' remained relatively high and stable, gradually decreasing with increasing frequency, which is characteristic of a dipolar dielectric system. At 1 mg L^{-1} concentration, ε' showed an anomalous peak at lower frequencies, reaching a maximum value around 6.5×10^5, indicative of pronounced interfacial polarization and enhanced dipole alignment. However, this sharp elevation was not sustained across the frequency range, and ε' dropped rapidly, suggesting unstable polarization behavior. In contrast, higher concentrations of 5 mg L^{-1} and 10 mg L^{-1} demonstrated a suppressed dielectric response, with consistently lower ε' values across all frequencies. This could be attributed to restricted dipole mobility and reduced space charge accumulation due to saturation or structural stiffening. Such frequency-dependent dispersion aligns well with the Maxwell–Wagner interfacial polarization model typically observed in biological tissues and heterogeneous composite materials. The loss tangent profile shown in Fig. 10(a) further reinforces the dielectric relaxation interpretation. The 1 mg L^{-1}-treated sample showed a dominant peak at low frequency, exceeding a value of 5, confirming significant energy dissipation due to interfacial losses and conductive relaxation processes. This peak then gradually diminished, suggesting a broad distribution of relaxation times. Meanwhile, the control and higher concentration samples displayed comparatively low and smooth loss tangent profiles with no prominent peaks, indicative of minimal dielectric losses and more stable dipole dynamics.

3.6 AC conductivity

The analysis of AC conductivity (σ_{ac}) offers critical insights into the frequency-driven charge transport mechanisms and polarization behavior within biological tissues.[59] In plant systems, such conductivity is primarily governed by ionic displacement and interfacial polarization phenomena.[60] The AC conductivity (σ_{ac}) of *Aloe vera* samples treated with varying concentrations of NCCH nanoparticles was assessed as a function of frequency and is plotted in Fig. 11 to understand the conduction behavior

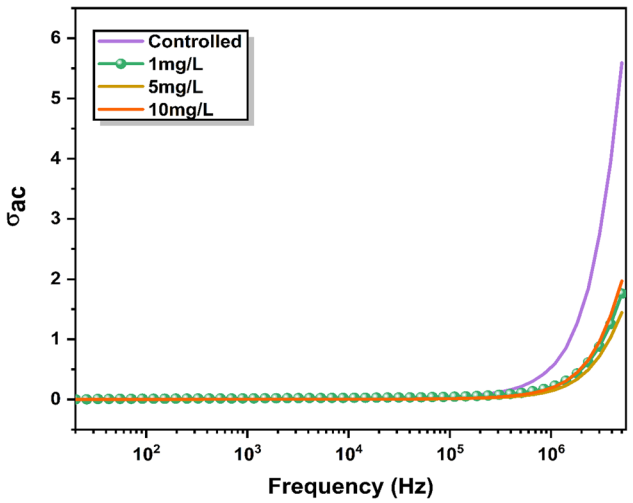

Fig. 11 Variation of AC conductivity (σ_{ac}) as a function of frequency for *Aloe vera* samples treated with different concentrations of NCCH (1 mg L^{-1}, 5 mg L^{-1}, and 10 mg L^{-1}) along with the control.

induced by nanoparticle incorporation. The total conductivity (σ_T) was calculated using the expression:

$$\sigma_T = \frac{\varepsilon_0 R}{C_0 |Z|^2}$$

where ε_0 is the permittivity of free space, R is the real part of impedance, C_0 is the geometrical capacitance, and $|Z|$ is the magnitude of impedance.

The frequency-dependent conductivity was described as eqn (6):

$$\sigma_T = \sigma_{ac}(\omega) = \sigma_{dc} + \sigma(\omega). \quad (6)$$

In this relation, σ_{dc} is the frequency-independent component associated with long-range charge transport and $\sigma(\omega)$ captures the dispersive behavior due to localized hopping mechanisms.

To model the dispersive region, Jonscher's universal power law was employed (eqn (7)):[61]

$$\sigma_{ac}(\omega) = \sigma_{dc} + A\omega^s. \quad (7)$$

Here, A is a pre-exponential factor and s is the frequency exponent that indicates the type of hopping conduction. A value of $0 < s < 1$ corresponds to translational hopping, typically observed in disordered biological systems, whereas $s > 1$ suggests localized or re-orientational hopping processes.[62] This model framework helps in interpreting the way NCCH nanoparticles influence charge carrier dynamics within the plant tissue, by altering both resistive and capacitive properties at the cellular and extracellular levels.

We observe that the σ_{ac} remains nearly constant in the low- to mid-frequency region, indicating the dominance of DC-like conduction behavior. As the frequency increases, a noticeable rise in σ_{ac} is observed, suggesting enhanced hopping conduction mechanisms at high frequencies. The trend is expected

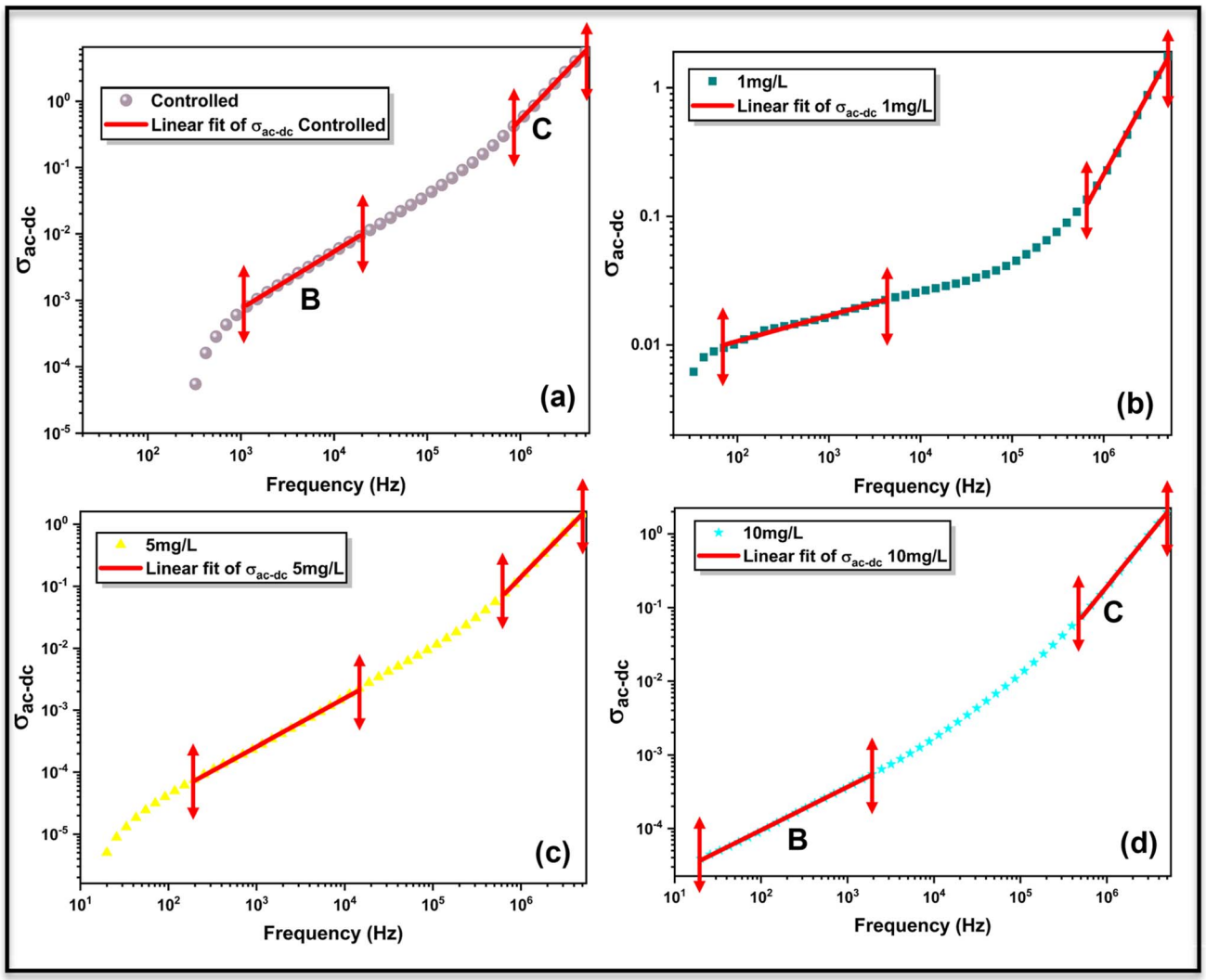

Fig. 12 Log–log plots showing the variation of frequency-dependent AC conductivity after subtracting the DC component ($\sigma_{ac}-\sigma_{dc}$) for *Aloe vera* samples treated with different concentrations of NCCH nanoparticles: (a) control, (b) 1 mg L^{-1}, (c) 5 mg L^{-1}, and (d) 10 mg L^{-1}. The fitted lines represent the Jonscher power law behavior, indicating distinct conduction zones.

from the power law and follows the literature available for *Aloe vera*.

The AC conductivity behavior of *Aloe vera* samples treated with different concentrations of NCCH was analyzed by plotting $\log(\sigma_{ac}(\omega)-\sigma_{dc})$ *versus* log(frequency), as shown in Fig. 12(a)–(d). The plot clearly reveals three distinct conduction regions. At low frequencies, the conductivity remains nearly constant, corresponding to the electrode interface effects. The mid-frequency region, labeled as region B, represents intercellular or grain boundary conduction, while the high-frequency region C corresponds to intracellular or grain conduction. A linear fit was applied to regions B and C to extract the Jonscher's parameters *s* and *A*, which describe the power-law dependence of AC conductivity.

From Table 2, it is observed that s_1 values for grain conduction are close to or above 1 for all samples, ranging from 1.29 to 1.47. Such values typically indicate a correlated barrier hopping (CBH) mechanism.[63] The highest s_1 (1.47) is found in the control and 5 mg L^{-1} samples, while the lowest s_1 (1.29) appears at 1 mg L^{-1}, suggesting some variation in charge carrier dynamics with treatment. In the grain boundary region (s_2), the values significantly decrease, particularly for the 1 mg L^{-1} sample (0.20), implying less correlated or even long-range hopping behavior in that region. The pre-exponential factor *A* also shows a noteworthy trend. For grain conduction (A_1), the values increase from 2.5×10^{-10} in the 5 mg L^{-1} sample to 3.9×10^{-9} in the 1 mg L^{-1} sample, indicating enhanced conductivity pathways possibly due to structural or compositional changes. In the grain boundary region, A_2 peaks sharply for 1 mg L^{-1} (4.0×10^{-3}), reinforcing the idea that the NCCH treatment alters charge transport through intercellular spaces. These findings confirm that NCCH treatment significantly modifies the conduction mechanisms in *Aloe vera* tissues, influencing both intra- and intercellular charge mobility.

The variation in the frequency exponent '*s*' and pre-exponential factor '*A*' with different NCCH concentrations

Table 2 Jonscher's parameters for AC conduction in grain and grain boundary

	Grain conduction			Grain boundary conduction		
Sample	s_1	A_1	R^2	s_2	A_2	R^2
Control	1.47 ± 0.011	$(7.41 \pm 0.056) \times 10^{-10}$	0.999	0.86 ± 0.007	$(2.0 \pm 0.009) \times 10^{-6}$	0.999
1 mg L^{-1}	1.29 ± 0.026	$(3.9 \pm 0.078) \times 10^{-9}$	0.996	0.20 ± 0.005	$(4 \pm 0.026) \times 10^{-3}$	0.987
5 mg L^{-1}	1.46 ± 0.008	$(2.5 \pm 0.0143) \times 10^{-10}$	0.999	0.78 ± 0.605	$(1.3 \pm 0.004) \times 10^{-6}$	0.998
10 mg L^{-1}	1.44 ± 0.01	$(4.49 \pm 0.034) \times 10^{-10}$	0.999	0.59 ± 0.003	$(6.3 \pm 0.01) \times 10^{-6}$	0.999

suggests that the electrical transport is dominated by a correlated barrier hopping (CBH) mechanism, with enhanced hopping activity at higher treatment levels. This reflects an increase in localized charge carrier dynamics, indicating that NCCH treatment modifies the microstructural and interfacial characteristics of the *Aloe vera* matrix, thereby influencing its dielectric and conductive behavior.

3.7 Electric modulus

The electric modulus formalism serves as an effective approach for exploring the electrical characteristics of low-capacitance materials.[64] Analysis of its frequency-dependent behaviour offers valuable insight into the relaxation dynamics governing charge transport within the system. This technique proves particularly useful in ionic systems, where changes in modulus are closely associated with the suppression of the electric field at a fixed dielectric displacement, thereby revealing the underlying conduction and relaxation mechanisms.[65]

As observed in Fig. 13(a), the real part of the modulus (M') remains low in the low-frequency region for all samples, indicating strong capacitive behavior due to interfacial polarization, which supports efficient energy storage. With increasing frequency, M' gradually increases, signifying a reduction in the ability of dipoles to follow the alternating field, thus reflecting the transition from capacitive to resistive response. The M' *versus* frequency curve for the 1 mg L^{-1} NCCH-treated *Aloe vera* sample displays distinctive nonlinear progression, particularly evident in the mid- to high-frequency region. At lower frequencies, M' remains subdued, reflecting strong interfacial polarization effects that limit field-induced charge displacement and indicate the dominance of space-charge accumulation at the electrode–tissue interface. However, as the frequency increases, a pronounced rise in M' is observed, marking a transition from interfacial polarization to bulk dielectric response. This sharp increase suggests that the 1 mg L^{-1} concentration promotes enhanced short-range ionic mobility and dielectric stiffness, potentially due to an optimal degree of particle–matrix interaction that facilitates localized energy storage without excessive structural disruption. The elevated slope compared to control further highlights the emergence of capacitive behavior at elevated frequencies, implying that NCCH at this dose modulates the electrical field response through improved dynamic alignment of dipolar and ionic species. On the other hand, 5 mg L^{-1} concentration shows the most linear and steady rise in M', suggesting a gradual energy storage build-up without pronounced relaxation. This could imply a more balanced

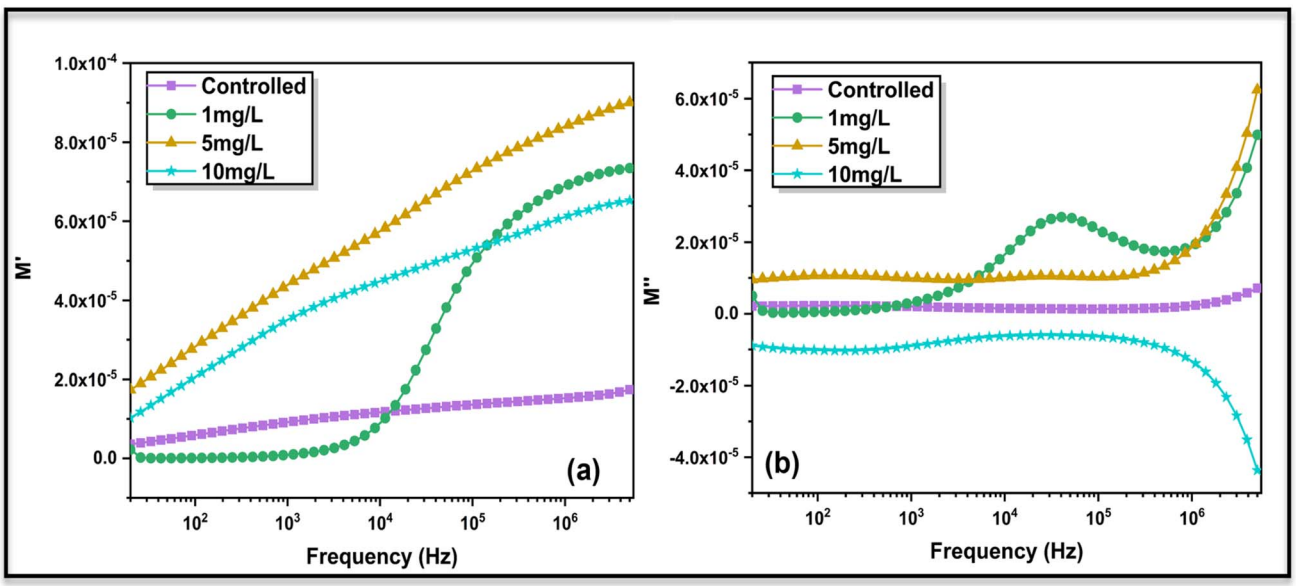

Fig. 13 Frequency-dependent variation of the real (a) and imaginary (b) parts of the electric modulus for *Aloe vera* samples treated with different concentrations of NCCH (1 mg L^{-1}, 5 mg L^{-1}, and 10 mg L^{-1}) along with the untreated control.

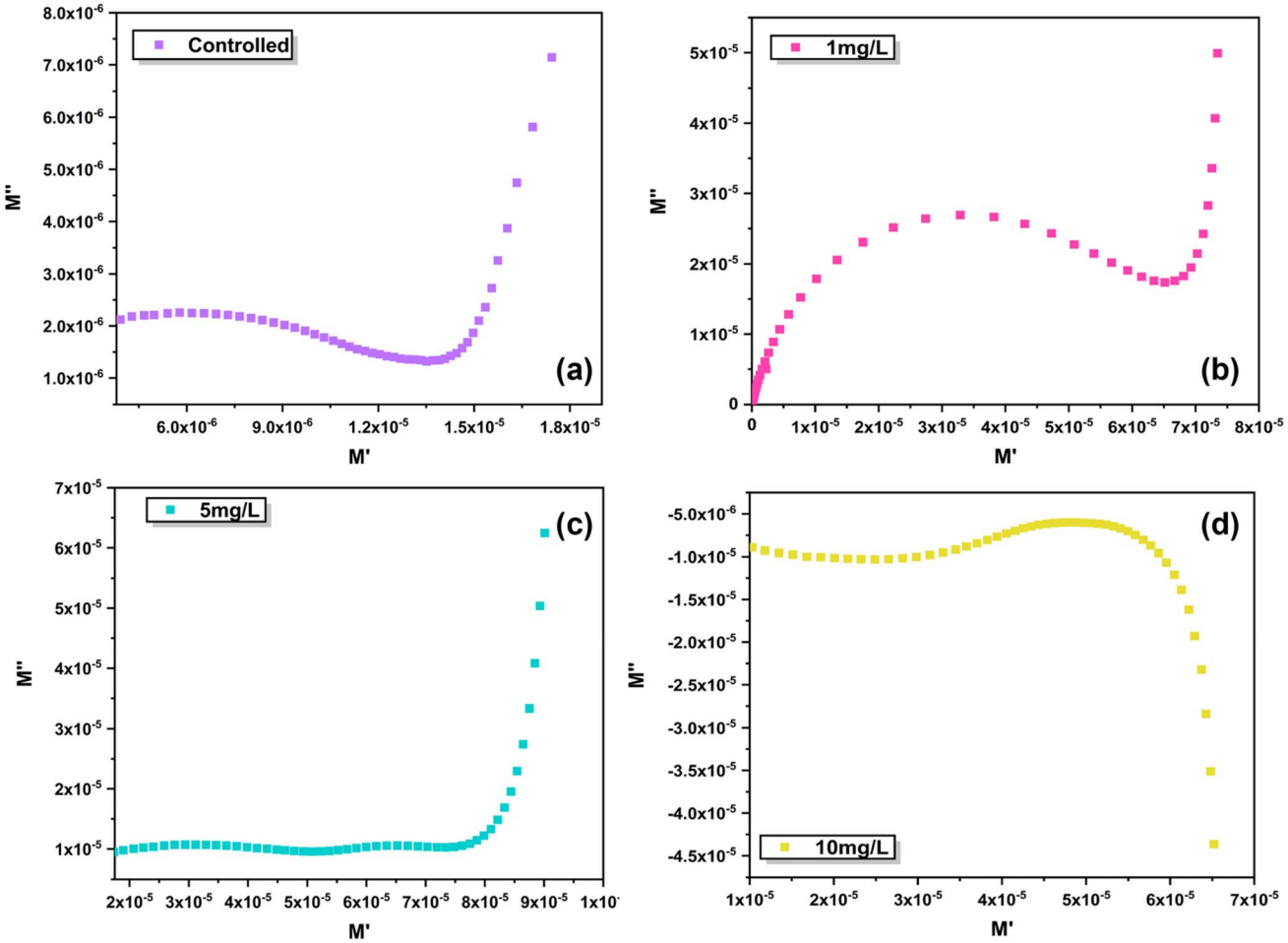

Fig. 14 Electric modulus spectra (M'' *vs.* M') of *Aloe vera* leaves treated with varying concentrations of NCCH nanoparticles: (a) control, (b) 1 mg L^{-1}, (c) 5 mg L^{-1}, and (d) 10 mg L^{-1}. The variation in semicircular arc shapes indicates changes in relaxation dynamics and dielectric behavior due to nanoparticle interaction with plant tissues.

carrier mobility and field interaction, making this concentration potentially ideal for sustained dielectric storage applications.

Fig. 13(b) shows a sharp peak in the imaginary part of the electric modulus (M'') for the 1 mg L^{-1} sample, suggesting the highly localized ionic motion and rapid relaxation processes, which could point to an optimal interaction level between the plant matrix and the NCCH particles. This behavior is not mirrored in the other concentrations, indicating a threshold-like effect where a small dose trigger enhanced short-range conduction. The 10 mg L^{-1} sample shows a negative shift in M'' at high frequencies, which is quite unusual. This may indicate capacitive overload or over-saturation of mobile carriers, possibly due to structural disturbance or excessive particle loading, reducing the capacity of material to polarize effectively.

The complex modulus plot (M' *vs.* M'') serves as a crucial diagnostic tool to assess the dielectric relaxation and energy storage behaviour within plant tissues subjected to varying external treatments. In these biopolymeric systems, such as *Aloe vera*, the arc profile generated in the M' *vs.* M'' graph reflects the dynamic response of polarizable species, particularly ionic and dipolar components, to the applied electric field. A distinct semicircular arc typically corresponds to a Debye-like relaxation process, indicative of homogeneous conduction pathways and minimal interfacial impedance, while deviations from this ideal form point toward complex relaxation dynamics, such as non-uniform charge mobility and localized field distortions.

In the current analysis, *Aloe vera* samples treated with different concentrations of NCCH nanoparticles exhibit contrasting M'–M'' profiles, revealing significant variations in their relaxation behaviour. The control sample, Fig. 14(a), shows a well-formed, symmetric arc, suggesting relatively uniform dielectric relaxation, indicative of stable ionic motion and structured charge storage. The 1 mg L^{-1} treated sample, Fig. 14(b), exhibits a larger and slightly elongated arc, highlighting enhanced dielectric relaxation. This implies increased ionic conductivity and better charge accommodation, likely due to the facilitation of ionic hopping mechanisms promoted by moderate NCCH interaction with the tissue matrix.

The 5 mg L^{-1} sample, Fig. 14(c), maintains an arc profile similar to the control, though slightly compressed, indicating

relatively preserved relaxation dynamics with minor alterations in ionic mobility. However, the most striking deviation is observed for the 10 mg L^{-1} treated sample, Fig. 14(d), where the M'' values drop into negative territory, forming an inverted arc. This anomaly suggests a severe disruption in the polarization mechanism, possibly caused by excessive nanoparticle accumulation leading to dielectric heterogeneity, charge trapping, or even localized field reversal effects. Such behaviour reflects compromised energy storage capability and points toward inefficient dielectric response at higher nanoparticle doses.

4. Conclusion

In this study, the electrical responses of freshly excised *Aloe vera* leaf tissues were systematically investigated upon exposure to bimetallic NCCH nanoparticles (NPs) at varying concentrations. Through impedance spectroscopy and comprehensive dielectric analyses, we unravelled key modifications in both the capacitive and conductive characteristics of the leaf tissue. The AC conductivity behaviour, modelled using Jonscher's power law, revealed a distinct suppression in σ_{ac} with increasing NP concentration, indicating a disruption in long-range charge transport pathways. This attenuation suggests that NCCH NPs modulate ionic mobility, most likely through interaction with membrane-bound or extracellular ionic carriers. Dielectric constant and loss tangent responses further substantiated these findings. The significant decline in permittivity at higher frequencies, especially in 10 mg L^{-1} treated samples, suggests reduced polarization capability, likely due to constrained dipolar orientation dynamics within the tissue microenvironment. Interestingly, the 1 mg L^{-1} treated sample exhibited a transient peak in tan δ, implying a unique regime of localized relaxation conducive to energy dissipation. Electric modulus analysis offered deeper insights into relaxation phenomena. Modulus spectra provided additional insights into charge relaxation. The imaginary part (M'') highlighted relaxation peaks for all treated samples except 10 mg L^{-1}, indicating suppressed ionic mobility at higher concentrations. M' *vs.* M'' plots showed closed arcs for control and lower doses, pointing to balanced energy storage and release behaviour, whereas the distorted arc at 10 mg L^{-1} reflected disrupted relaxation dynamics. Overall, this work highlights that NCCH nanoparticles significantly modulate the electrical response of *Aloe vera* in a concentration-dependent manner. The 1 mg L^{-1} treatment showed enhanced short-range ionic activity, while 10 mg L^{-1} impaired both charge transport and relaxation. These findings emphasize the potential of using engineered nanomaterials like NCCH to tailor plant's electrical and physiological responses, with possible applications in plant sensing, energy modulation, and nano-enabled agriculture.

Author contributions

K. G. wrote the original manuscript, performed the synthesis and characterization experiments, and conducted complete data analysis. M. B. reviewed and edited the manuscript, provided key suggestions related to the chemistry of the NCCH material, assisted in the analysis of XRD, FTIR, and TEM data, and data collection. A. S. reviewed and edited the manuscript and provided essential resources. H. S. reviewed and edited the manuscript and provided essential resources. A. K. S. supervised the overall work, reviewed and edited the manuscript, and assisted in data analysis.

Conflicts of interest

The authors declare that there are no conflicts of interest regarding the publication of this paper.

Data availability

The datasets generated during and/or analysed during the current study are available from the corresponding author upon reasonable request.

Acknowledgements

The authors express their sincere gratitude to the Research & Development department at UPES Dehradun for providing the necessary research facilities to support this work. The authors also thank ADXRD Beamline (BL-12), Indus-2, RRCAT, Indore, India, for providing synchrotron beamtime and support. KG and MB acknowledge UPES for providing Research Fellowship.

References

1 F. Zhao, Y. Zhao, Y. Liu, X. Chang, C. Chen and Y. Zhao, Cellular Uptake, Intracellular Trafficking, and Cytotoxicity of Nanomaterials, *Small*, 2011, **7**(10), 1322–1337.
2 S. Ali, A. Mehmood and N. Khan, Uptake, Translocation, and Consequences of Nanomaterials on Plant Growth and Stress Adaptation, *J. Nanomater.*, 2021, **2021**, 6677616, DOI: 10.1155/2021/6677616.
3 S. K. Patra, R. Poddar, M. Brestic, P. U. Acharjee, P. Bhattacharya, S. Sengupta, P. Pal, N. Bam, B. Biswas, V. Barek, P. Ondrisik, M. Skalicky and A. Hossain, Prospects of Hydrogels in Agriculture for Enhancing Crop and Water Productivity under Water Deficit Condition, *Int. J. Polym. Sci.*, 2022, **2022**(1), 4914836, DOI: 10.1155/2022/4914836.
4 W. Zaman, A. Ayaz and S. Park, Nanomaterials in Agriculture: A Pathway to Enhanced Plant Growth and Abiotic Stress Resistance, *Plants*, 2025, **14**(5), 716.
5 K. Gunawardena and K. Steemers, Living Walls in Indoor Environments, *Build. Environ.*, 2019, **148**, 478–487.
6 C. Chiang, D. Bånkestad and G. Hoch, Reaching Natural Growth: Light Quality Effects on Plant Performance in Indoor Growth Facilities, *Plants*, 2020, **9**(10), 1273.
7 L. Wang, M. Xiao, X. Guo, Y. Yang, Z. Zhang and C. Lee, Sensing Technologies for Outdoor/Indoor Farming, *Biosensors*, 2024, **14**(12), 629.
8 G. Dufil, I. Bernacka-Wojcik, A. Armada-Moreira and E. Stavrinidou, Plant Bioelectronics and Biohybrids: The

Growing Contribution of Organic Electronic and Carbon-Based Materials, *Chem. Rev.*, 2021, **122**(4), 4847–4883.

9 T. T. S. Lew, V. B. Koman, P. Gordiichuk, M. Park and M. S. Strano, The Emergence of Plant Nanobionics and Living Plants as Technology, *Adv. Mater. Technol.*, 2020, **5**(3), 1900657, DOI: **10.1002/admt.201900657**.

10 K. S. Siddiqi and A. Husen, Plant Response to Engineered Metal Oxide Nanoparticles, *Nanoscale Res. Lett.*, 2017, **12**, 1–18.

11 U. Krämer, I. N. Talke and M. Hanikenne, Transition Metal Transport, *FEBS Lett.*, 2007, **581**(12), 2263–2272, DOI: **10.1016/j.febslet.2007.04.010**.

12 O. S. Ayanda, A. O. Mmuoegbulam, O. Okezie, N. I. Durumin Iya, S. E. Mohammed, P. H. James, A. B. Muhammad, A. A. Unimke, S. A. Alim and S. M. Yahaya, Recent Progress in Carbon-Based Nanomaterials: Critical Review, *J. Nanopart. Res.*, 2024, **26**(5), 106.

13 A. O. Egbedina, O. P. Bolade, U. Ewuzie and E. C. Lima, Emerging Trends in the Application of Carbon-Based Materials: A Review, *J. Environ. Chem. Eng.*, 2022, **10**(2), 107260.

14 Y. Cui, K. Wang and C. Zhang, Carbon Nanomaterials for Plant Priming through Mechanostimulation: Emphasizing the Role of Shape, *ACS Nano*, 2024, **18**(16), 10829–10839.

15 D. Wang and D. Astruc, The Recent Development of Efficient Earth-Abundant Transition-Metal Nanocatalysts, *Chem. Soc. Rev.*, 2017, **46**(3), 816–854.

16 R. Vatansever, I. I. Ozyigit and E. Filiz, Essential and Beneficial Trace Elements in Plants, and Their Transport in Roots: A Review, *Appl. Biochem. Biotechnol.*, 2017, **181**(1), 464–482, DOI: **10.1007/s12010-016-2224-3**.

17 M. Bhatt, A. Sinha, P. Bhojane, M. Singh and M. Gupta, Structural and Electronic Properties of Nickel–Cobalt Carbonate Hydroxide Hydrate Nanostructures for High Performance Supercapacitor Applications, *J. Mater. Sci.: Mater. Electron.*, 2023, **34**(28), 1933.

18 M. Bhatt, B. Gupta and A. Sinha, Superior Charge Storage Performance of Optimized Nickel Cobalt Carbonate Hydroxide Hydrate Nanostructures for Supercapacitor Application, *Sci. Rep.*, 2025, **15**(1), 2192.

19 N. Singh, Z. Iqbal, T. A. Ansari, M. A. Khan, N. Ali, A. Khan and M. Singh, The Portent Plant with a Purpose: Aloe Vera, *J. Pharmacogn. Phytochem.*, 2019, **8**(3), 4124–4130.

20 K. M. Katubi, A. Amari, H. N. Harharah, M. M. Eldirderi, M. A. Tahoon and F. Ben Rebah, Aloe Vera as Promising Material for Water Treatment: A Review, *Processes*, 2021, **9**(5), 782.

21 J. Delatorre-Herrera, I. Delfino, C. Salinas, H. Silva and L. Cardemil, Irrigation Restriction Effects on Water Use Efficiency and Osmotic Adjustment in Aloe Vera Plants (Aloe Barbadensis Miller), *Agric. Water Manag.*, 2010, **97**(10), 1564–1570.

22 K. Gautam, M. Bhatt, S. Dutt, A. Sagdeo and A. K. Sinha, Impact of Carbon Nanodot Uptake on Complex Impedance Charge Transport and Energy Storage Mechanism in Aloe Vera Leaves, *Sci. Rep.*, 2025, **15**(1), 11506, DOI: **10.1038/s41598-025-96430-8**.

23 D. Lin and B. Xing, Root Uptake and Phytotoxicity of ZnO Nanoparticles, *Environ. Sci. Technol.*, 2008, **42**(15), 5580–5585, DOI: **10.1021/es800422x**.

24 A. Chahardoli, N. Karimi, X. Ma and F. Qalekhani, Effects of Engineered Aluminum and Nickel Oxide Nanoparticles on the Growth and Antioxidant Defense Systems of Nigella Arvensis L., *Sci. Rep.*, 2020, **10**(1), 3847, DOI: **10.1038/s41598-020-60841-6**.

25 P. M. G. Nair, S.-H. Kim and I. M. Chung, Copper oxide nanoparticle toxicity in mung bean (Vigna radiata L.) seedlings: physiological and molecular level responses of in vitro grown plants Acta Physiologiae Plantarum 2014 2947-2958, *Acta Physiol. Plant.*, 2014, **36**, 2947–2958, DOI: **10.1007/s11738-014-1667-9**.

26 S. H. Lee, H. Seo, H. S. Lee and Y. Park, Development and characterization of a human cell line-based transactivation assay to assess thyroid EDCs, *Cryst. Struct. Commun.*, 2020, **36**(1), 109110, DOI: **10.1016/j.envres.2020.109110**.

27 P. Bhojane, A. Le Bail and P. M. SHirage, A Quarter of a Century after Its Synthesis and With> 200 Papers Based on Its Use,Co (CO3) 0.5 (OH)· 0.11 H2O′ Proves to Be Co6 (CO3) 2 (OH) 8· H2O from Synchrotron Powder Diffraction Data, *Cryst. Struct. Commun.*, 2019, **75**(1), 61–64, DOI: **10.1107/S2053229618017734**.

28 M. Djanaguiraman, V. Anbazhagan, O. P. Dhankher and P. V. Prasad, Uptake, Translocation, Toxicity, and Impact of Nanoparticles on Plant Physiological Processes, *Plants*, 2024, **13**(22), 3137.

29 T. Isaacs, The Mineralogy and Chemistry of the Nickel Carbonates, *Mineral. Mag. J. Mineral. Soc.*, 1963, **33**(263), 663–678.

30 A. Pathak and D. Maity, Distinctive IR Signature of $CO_3^{\bullet-}$ and CO_3^{2-} Hydrated Clusters: A Theoretical Study, *J. Phys. Chem. A*, 2009, **113**(48), 13443–13447.

31 Y. Budipramana, T. Ersam and F. Kurniawan, Synthesis Nickel Hydroxide by Electrolysis at High Voltage, *ARPN J. Eng. Appl. Sci.*, 2014, **9**(11), 2074–2077.

32 H. Du, C. T. Williams, A. D. Ebner and J. A. Ritter, In Situ FTIR Spectroscopic Analysis of Carbonate Transformations during Adsorption and Desorption of CO_2 in K-Promoted HTlc, *Chem. Mater.*, 2010, **22**(11), 3519–3526.

33 M. Shabanian, N. Basaki, H. A. Khonakdar, S. H. Jafari, K. Hedayati and U. Wagenknecht, Novel Nanocomposites Consisting of a Semi-Crystalline Polyamide and Mg–Al LDH: Morphology, Thermal Properties and Flame Retardancy, *Appl. Clay Sci.*, 2014, **90**, 101–108.

34 E. A. Price, N. I. Hammer and M. A. Johnson, A Cluster Study of Cl_2^- Microhydration: Size-Dependent Competition between Symmetrical H-Bonding to the Anion and the Formation of Cyclic Water Networks in the $Cl_2^-\cdot 1{-}5(H_2O)$ Series, *J. Phys. Chem. A*, 2004, **108**(18), 3910–3915.

35 D. Bajer, K. Janczak and K. Bajer, Novel Starch/Chitosan/Aloe Vera Composites as Promising Biopackaging Materials, *J. Polym. Environ.*, 2020, **28**(3), 1021–1039.

36 S. Kumar, M. Yadav, A. Yadav and J. Yadav, Impact of Spatial and Climatic Conditions on Phytochemical Diversity and in

Vitro Antioxidant Activity of Indian Aloe Vera (L.) Burm.f., *S. Afr. J. Bot.*, 2017, **111**, 50–59.

37 F. Dai, Q. Zhuang, G. Huang, H. Deng and X. Zhang, Infrared Spectrum Characteristics and Quantification of OH Groups in Coal, *ACS Omega*, 2023, **8**(19), 17064–17076.

38 M. Raula, M. H. Rashid, S. Lai, M. Roy and T. K. Mandal, Solvent-Adoptable Polymer Ni/NiCo Alloy Nanochains: Highly Active and Versatile Catalysts for Various Organic Reactions in Both Aqueous and Nonaqueous Media, *ACS Appl. Mater. Interfaces*, 2012, **4**(2), 878–889, DOI: **10.1021/am201549a**.

39 S. Torres-Giner, S. Wilkanowicz, B. Melendez-Rodriguez and J. M. Lagaron, Nanoencapsulation of Aloe Vera in Synthetic and Naturally Occurring Polymers by Electrohydrodynamic Processing of Interest in Food Technology and Bioactive Packaging, *J. Agric. Food Chem.*, 2017, **65**(22), 4439–4448.

40 J. Liu, Q. Zhang, F. Ma, S. Zhang, Q. Zhou and A. Huang, Three-Step Identification of Infrared Spectra of Similar Tree Species to Pterocarpus Santalinus Covered with Beeswax, *J. Mol. Struct.*, 2020, **1218**, 128484.

41 S. T. L. Jales, R. d. M. Barbosa, G. R. da Silva, P. Severino and T. F. A. de Lima Moura, Natural Polysaccharides from Aloe Vera L. Gel (Aloe Barbadensis Miller): Processing Techniques and Analytical Methods, *Polysacch. Prop. Appl.*, 2021, 1–22.

42 M. A. López-Mata, M. Gastelum-Cabrera, E. Valbuena-Gregorio, P. B. Zamudio-Flores, S. E. Burruel-Ibarra, G. G. Morales-Figueroa, L. Quihui-Cota and J. E. Juárez-Onofre, Physicochemical Properties of Novel Pectin/Aloe Gel Membranes, *Iran. Polym. J.*, 2018, **27**, 545–553.

43 M. I. Hussain, A. El-Keblawy, N. Akhtar and A. S. Elwakil, Electrical Impedance Spectroscopy in Plant Biology, in *Sustainable Agriculture Reviews 52*, ed. E. Lichtfouse, Springer International Publishing, Cham, 2021, pp. 395–416, DOI: **10.1007/978-3-030-73245-5_12**.

44 A. G. Volkov, J. C. Foster, E. Jovanov and V. S. Markin, Anisotropy and Nonlinear Properties of Electrochemical Circuits in Leaves of Aloe Vera L., *Bioelectrochemistry*, 2011, **81**(1), 4–9.

45 M. V. Nikolic, C. Singh and M. Bogdanovic, Exploration of the Charge Transport Mechanism, Complex Impedance, Dielectric/Electric Modulus and Energy Storage Characteristics of the Aloe Vera (Aloe Barbadensis Miller) Plant, *Mater. Res. Express*, 2024, **11**(1), 016302, DOI: **10.1088/2053-1591/ad1b03**.

46 K. Kadan-Jamal, M. Sophocleous, A. Jog, D. Desagani, O. Teig-Sussholz, J. Georgiou, A. Avni and Y. Shacham-Diamand, Electrical Impedance Spectroscopy of Plant Cells in Aqueous Biological Buffer Solutions and Their Modelling Using a Unified Electrical Equivalent Circuit over a Wide Frequency Range: 4 Hz to 20 GHz, *Biosens. Bioelectron.*, 2020, **168**, 112485, DOI: **10.1016/j.bios.2020.112485**.

47 S. Karmakar, Impedance Spectroscopy for Electroceramics and Electrochemical System, *arXiv*, 2024, preprint, arXiv:2406.15467, DOI: **10.48550/arXiv.2406.15467**.

48 P. Córdoba-Torres, Relationship between Constant-Phase Element (CPE) Parameters and Physical Properties of Films with a Distributed Resistivity, *Electrochim. Acta*, 2017, **225**, 592–604.

49 S. Singh, A. Kaur, P. Kaur and L. Singh, High-Temperature Dielectric Relaxation and Electric Conduction Mechanisms in a $LaCoO_3$-Modified $Na_{0.5}Bi_{0.5}TiO_3$ System, *ACS Omega*, 2023, **8**(28), 25623–25638, DOI: **10.1021/acsomega.3c04490**.

50 S. M. Gateman, O. Gharbi, H. G. De Melo, K. Ngo, M. Turmine and V. Vivier, On the Use of a Constant Phase Element (CPE) in Electrochemistry, *Curr. Opin. Electrochem.*, 2022, **36**, 101133.

51 Z. Gong, W. Zhao, K. Guan, P. Rao, Q. Zeng, J. Liu and Z. Feng, Influence of Grain Boundary and Grain Size on the Mechanical Properties of Polycrystalline Ceramics: Grain-scale Simulations, *J. Am. Ceram. Soc.*, 2020, **103**(10), 5900–5913.

52 T. Defferriere, D. Klotz, J. C. Gonzalez-Rosillo, J. L. Rupp and H. L. Tuller, Photo-Enhanced Ionic Conductivity across Grain Boundaries in Polycrystalline Ceramics, *Nat. Mater.*, 2022, **21**(4), 438–444.

53 S. W. Fanta, M. K. Abera, Q. T. Ho, P. Verboven, J. Carmeliet and B. M. Nicolai, Microscale Modeling of Water Transport in Fruit Tissue, *J. Food Eng.*, 2013, **118**(2), 229–237.

54 M. Chang, D. Stout and J. Willison, Electrical Impedance Analysis in Plant Tissues: Symplasmic Resistance and Membrane Capacitance in the Haydon Model, *J. Exp. Bot.*, 1990, **41**, 371–380.

55 K. S. Cole and R. H. Cole, Dispersion and Absorption in Dielectrics II. Direct Current Characteristics, *J. Chem. Phys.*, 1942, **10**(2), 98–105.

56 A. B. Itolikar, A. S. Joshi, A. R. Deshmukh and A. C. Kumbharkhane, Frequency and Temperature-Dependent Dielectric Behaviour of Fresh Aloe Vera at 1 to 20 GHz Microwave Frequency Using Time Domain Reflectometry, *Horizon*, 2024, **11**(4), 1078–1082, DOI: **10.14719/pst.3927**.

57 H. Zhang, H. Tan and S. Jiang, Fundamentals of Dielectric Materials for Capacitive Energy Storage, *Dielectric Materials for Capacitive Energy Storage*, Taylor & Francis Group, Boca Raton, 2024, pp. 1–25, **https://doi.org/10.1201/9781003454496**.

58 M. A. Alsaiari, M. Morsy, M. Samir, A. Al-Qahtani, R. Aslsaiari, A. Alsaiari, E. A. Kamoun, A. I. Ali and G. H. Ramzy, Advantages Incorporating V_2O_5 Nanoparticles into PMMA Composite Membranes for the Structural, Optical, Electrical, and Mechanical Properties for Conductive Polymeric Membrane Applications, *Mater. Adv.*, 2024, **5**(8), 3297–3308.

59 B. J. Roth, The Electrical Conductivity of Tissues, *Biomed. Eng. Handb.*, 2000, **1**, 10–11.

60 A. H. Calori, T. L. Factor, J. C. Feltran, E. Y. Watanabe, C. C. d. Moraes and L. F. V. Purquerio, Seed Potato Minituber Production in an Aeroponic System under Tropical Conditions: Electrical Conductivity and Plant Density, *J. Plant Nutr.*, 2018, **41**(17), 2200–2209.

61 A. Jonscher, Frequency-Dependence of Conductivity in Hopping Systems, *J. Non-Cryst. Solids*, 1972, **8**, 293–315.
62 H. Hussein, S. Ibrahim and S. A. Khairy, Eco-Friendly $CoFe_2O_4$ Ferrite Nanoparticles Prepared Using Greek Yogurt Solution: Deep Insights into Optical Properties and Abnormal Semiconductor–Insulator–Semiconductor Transitions for Optoelectronics and Catalytic Applications, *Mater. Adv.*, 2025, **6**(7), 2297–2327.
63 Y. Ben Taher, A. Oueslati, N. K. Maaloul, K. Khirouni and M. Gargouri, Conductivity Study and Correlated Barrier Hopping (CBH) Conduction Mechanism in Diphosphate Compound, *Appl. Phys. A*, 2015, **120**(4), 1537–1543, DOI: 10.1007/s00339-015-9353-3.
64 B. M. Melo, C. Baivier, R. Benzerga, D. Fasquelle, S. S. Teixeira, M. P. Graça and L. Costa, $BaTiO_3$—$Gd_3Fe_5O_{12}$ Composites: Exploring the Dielectric Properties in a Broad Frequency Range, *Crystals*, 2024, **14**(7), 590.
65 R. A. Raj, A. Joseph, S. Hussain, M. Fahad, T. Maity, P. Sarun and L. K. Joy, Frequency and Temperature Dependent Dielectric Properties of $CoFe_{2-x}Y_xO_4$: Polarization and Conduction Mechanisms Pertained to Crystallographic Symmetry and Electronic Transitions, *J. Mater. Chem. C*, 2025, **13**, 5880–5910, DOI: 10.1039/D4TC04677C.